

Factorized electron-nuclear dynamics with effective complex potential: on-the-fly implementation for H_2^+ in a laser field

Julian Stetzler, Sophya Garashchuk,* and Vitaly Rassolov†

*Department of Chemistry & Biochemistry,
University of South Carolina, Columbia, South Carolina 29208*

(Dated: October 10, 2025)

Abstract

Conventional theoretical and computational approaches to fully coupled quantum molecular dynamics, i.e. when both the electrons and nuclei are treated as quantum-mechanical particles, are impractical for all but the smallest chemical systems. In this paper we describe the formalism and implementation of the Factorized Electron Nuclear Dynamic (FENDy) with effective complex potential [J. Chem. Theory Comput. **19** (2023), pp 1393-1408], which goes beyond the established framework of the Born-Oppenheimer approximation or Born-Huang expansion of the molecular wavefunction. This method is based on the exact factorization of the molecular wavefunction, with the nuclei evolving under a complex time-dependent potential which captures the key features of dynamics in the nuclear subspace. The complementary electronic component of the molecular wavefunction is normalized to one for all nuclear configurations. We implement and employ FENDy to model the dynamics of H_2^+ molecular ion under a femtosecond laser pulse. The electronic wavefunction is represented within the standard electronic structure bases without referencing the electronic eigenstates. The nuclear wavefunction is represented as a quantum-trajectory ensemble, which in principle circumvents the exponential scaling of the numerical cost with the system size. The challenging evaluation of the gradients on unstructured grids is performed by projection on auxiliary bases.

Keywords:

Quantum dynamics; exact factorization; H_2^+ photoionization; complex potential

* garashchuk@sc.edu

† rassolov@mailbox.sc.edu

I. INTRODUCTION

One of '33 Unresolved Questions in Nanoscience and Nanotechnology' posed by the authors in a recent focus article in ACS Nano [1] is "How can we model materials across length scales where classical or quantum mechanics alone are inadequate to match theory and experiment?" Such quantum/classical delineation is typically understood as 'capturing electronic properties of small systems' with quantum mechanics, while 'modeling larger systems using empirical or quantum-derived forces' with classical molecular dynamics, i.e. trajectories, and Monte Carlo methods [1]. While both frameworks provide fundamental insights into the properties and behavior of molecular systems, current experiments and theories, e.g. those focused on coherent and strongly coupled quantum motion of the nuclei, plasmons and light [2–5], go well beyond the above-mentioned quantum/classical separation of time- and length-scales associated with electrons and nuclei or atoms, respectively. However, there is no established theoretical framework which readily incorporates the nuclear quantum effects (NQE) into the trajectory dynamics of large molecular systems, combined with the spatially 'localized' description of electronic wavefunctions as wavepackets consisting of hundreds and thousands of electronic eigenstates. Some recent theoretical studies involving hundreds of electronic states include, for example, behavior plasmonic silver–platinum nanoparticles in photocatalysts [6], nonradiative exciton dynamics in monolayer black phosphorus [7], and soft x-ray near-edge spectra in transition metal complexes [8], while simulation of plasmons in nanorods of up to 2160 silver atoms extend to 24,000 electrons[9]. When it comes to the quantum behavior of the nuclei, the NQEs are most often associated with motion of light particles, such as protons and their isotopologues [10], though quantum tunneling of heavy atoms is gaining recognition as well (e.g. the heavy atom tunneling associated with the ring expansion of fluorenylazirines [11]). Recent state-of-the-art rigorous quantum dynamics studies (implemented in up to 12 dimensions) based on stationary basis or discrete variable representations [12] of nuclear wavefunctions and sophisticated contraction schemes, helped explain experiments involving molecules and clusters in gas phase and in confinement [13–17]. However, given the exponential scaling of exact methods with the system size and the need to include NQEs and multiple electronic states, motivates theoretical development departing from the basis description of the nuclear wavefunctions and the Born-Huang representation of the molecular wavefunction [18].

One such development is the exact factorization (XF) method, introduced into theoretical chemistry by Abedi, Maitra and Gross in 2010 [19]. The XF is an approach to quantum molecular dynamics based on the product form of time-dependent multi-component wavefunctions, which for clarity of discussion here will be taken as the electron-nuclear wavefunction,

$$\Psi(\mathbf{R}, q, t) = \underbrace{\psi(q, t)}_{\text{nuclear}} \underbrace{\Phi(\mathbf{R}, q, t)}_{\text{electronic}},$$

subject to the partial normalization condition of Φ in the electronic space. Here, vector \mathbf{R} represents electronic coordinates. The electronic wavefunction is normalized to 1, $\langle \Phi | \Phi \rangle_{\mathbf{R}} = 1$, for any configuration of the nuclei, denoted here as a single coordinate q , at all times, t . For such factorization to be 'exact', the electronic component, Φ , has to be a function of both the electronic and nuclear coordinates. The XF representation can be viewed as a way of dealing with large numbers of electronic states, by $\Phi(\mathbf{R}, q, t)$ being an electronic wavepacket, and as a starting point for well-defined approximations to the dynamics of both wavefunction components, necessary for applications to large molecular systems.

Recent theoretical developments in XF include extensions to polaritonic chemistry [20–22], a new XF-based theory of electronic friction [23], and the factorized electron-nuclear dynamics (FENDy) with a complex potential [24]. One major application of XF ideas was the development of the Coupled Trajectory-Mixed Quantum Classical (CT-MQC) method [25]. Further applications include decoherence corrections derived from the XF to augment surface hopping. These methods were recently added to the Libra software package for use with both model and atomistic systems [26].

To the best of our knowledge, the largest chemical application to date is the study of the ring-opening of oxirane, where the approximate CT-MQC method was applied to a realistic molecular system using on-the-fly Density Functional Theory computation of the electronic structure [27–30]. However, when it comes to use of XF as an exact method applications are limited to small model systems, such as Tully models [24, 31], one-dimensional H_2^+ in a laser field with soft coulomb interactions [32, 33], and the Shin-Metiu [34, 35] model where accurate solutions on the full-space can be used to construct the XF wavefunctions. In these studies, XF provided conceptual understanding of molecular Berry phases [36], and the forces driving nuclear dynamics in non-adiabatic systems [37, 38]. The reason is that the numerical solution of the coupled electronic and nuclear Schrödinger equations within the XF, presents major challenges associated the singularity of the non-classical momentum, $r(q, t)$,

$$r(q, t) := \frac{\nabla_q |\psi(q, t)|}{|\psi(q, t)|},$$

in the regime of diverging XF nuclear probability density, $|\psi(q, t)|^2$, and in the low-amplitude regions of $\psi(q, t)$, the latter due to the partial normalization condition of the electronic wavefunction $\Phi(\mathbf{R}, q, t)$ imposed at *all* q . The origin and handling of the singularity in $r(q, t)$, including the use of masking functions as a way of reducing the associated noise [39] were recently discussed in the literature [40, 41].

In this paper we report the first implementation of the factorized electron-nuclear dynamics with complex potential in the nuclear subspace for the H_2^+ molecule, which has been widely studied as a model system for electron-nuclear dynamics with photoexcitations. [42–53]. We employ the basis description of an electron (3 DOFs) interacting with two protons via the Coulomb potential. The nuclear XF wavefunction is represented by the quantum trajectory ensemble – an approach which is potentially scalable to large systems [54] – and the system is subjected to a laser pulse leading to photodissociation of H_2^+ .

In the remainder of this paper, Section II presents the model and theoretical background. Details of implementation are described in Section III; the results and discussion are given in Section IV; Section V gives a summary and outlook.

II. THEORY

For clarity we will first introduce the molecular model, and then present the theoretical approach using notations specific to the model. Cursive bold letters denote vectors, while capital bold letters are reserved for the matrices. Generalization of the theory to multidimensional nuclear subspace can be found in Refs [19, 24]. Integration over the electronic subspace is denoted $\langle \dots \rangle_{\mathbf{R}}$.

Model parameters (a.u.)				
$M = 918.076336$	$\varepsilon = 0.035$	$t_0 = 40$	$\alpha = 0.01$	$\omega = 0.420604544$

TABLE I. The model parameters used for the numeric analysis. M is the reduced mass of the two protons. The remaining parameters define the laser pulse. The frequency of the laser is ω and corresponds to a wavelength of 106 nm; its peak intensity is ε giving an intensity on the order 10^{14} W/cm² in SI units occurring at time t_0 . The envelope width α is about 40 a.u.

A. The Model

We will consider dynamics of H_2^+ – a system comprised of one electron and two protons – subjected to a laser field. The system is described in the internal molecular coordinate q , that describes the bond length, with no rotation. With that the total Hamiltonian (in atomic units) is

$$\hat{H} = -\frac{1}{2M} \nabla_q^2 + \hat{H}^{BO} + \hat{V}^{ext}(\mathbf{R}, q, t), \quad (1)$$

where \hat{H}^{BO} is the usual Born-Oppenheimer electronic hamiltonian,

$$\hat{H}^{BO} := -\frac{1}{2} \nabla_{\mathbf{R}}^2 - \frac{1}{\sqrt{x^2 + y^2 + (z + q/2)^2}} - \frac{1}{\sqrt{x^2 + y^2 + (z - q/2)^2}} + \frac{1}{q}. \quad (2)$$

The vector $\mathbf{R} = (x, y, z)$ denotes the electrons in full three-dimensional Cartesian coordinates, and M is the reduced mass of the nuclei. The external potential, $\hat{V}^{ext}(\mathbf{R}, q, t)$, is the laser field in the length gauge. It is defined as the scalar product of the electric field vector, $\mathbf{E}(t)$, and the electronic coordinate \mathbf{R} . The electric field is taken as a monochromatic beam in a Gaussian envelope along the electronic z -direction (along the bond axis),

$$\mathbf{E}(t) = \left(0, 0, \varepsilon e^{-\alpha(t-t_0)^2} \sin(\omega t)\right), \quad (3)$$

yielding

$$\hat{V}^{ext}(\mathbf{R}, q, t) = \mathbf{E}(t) \cdot \mathbf{R} = \varepsilon z e^{-\alpha(t-t_0)^2} \sin(\omega t). \quad (4)$$

The numerical values of the parameters, given in Table I, correspond to a femtosecond (approx 40 a.u.) laser pulse with a wavelength of 106 nm and a peak intensity on the order of 10^{14} W/cm². The length of the pulse is defined by the width of the gaussian envelope α and the wavelength by the frequency ω . The parameter ε defines the peak intensity and t_0 defines the time of peak intensity. This model allows us to examine the effect of the electron-nuclear coupling on dynamics directly by working without approximations to the electron correlation necessary for multi-electron systems, while the electron is described within standard basis sets of quantum chemistry.

B. The exact factorization approach with complex nuclear potential

In this section we outline the exact factorization (XF) formalism, specifically FENDy presented in Ref. [24]. A notable difference between FENDy and the XF framework introduced by Abedi, Maitra and Gross [19], is that the former is based on the complex scalar

potential rather than on the vector potential. The XF formalism is based on the product form of the electron-nuclear wavefunction $\Psi(\mathbf{R}, q, t)$,

$$\Psi(\mathbf{R}, q, t) = \psi(q, t)\Phi(\mathbf{R}, q, t), \quad (5)$$

where $\psi(q, t)$ is the purely *nuclear* component and $\Phi(\mathbf{R}, q, t)$ is the *electronic* component. The latter satisfies the partial normalization condition, i.e. it is normalized to one for any configuration of the nuclei,

$$\langle \Phi | \Phi \rangle_{\mathbf{R}} = 1 \text{ for all } q \text{ and } t. \quad (6)$$

For Eq. (5) to be formally exact, the 'electronic' component Φ is a function of all spatial coordinates, \mathbf{R} , q , and of time, t , just as the full molecular wavefunction Ψ . Yet, the XF representation of Ψ offers the following potential advantages. If the nuclear dynamics is largely captured by $\psi(y, t)$, then (i) the resulting electron-nuclear terms might be small and, thus, amenable to approximations. (ii) The nuclear dynamics may be treated approximately, for example, using an ensemble of semiclassical or quantum trajectories. Such description of the nuclear DOFs may allow to circumvent the formal exponential scaling with the system size even for large amplitude motion, while retaining the dominant NQEs. (iii) The resulting time-dependent Schrödinger equation (TDSE) on Φ , coupled to propagation of ψ , could be solved without explicit reference to the electronic eigenstates, treating Φ as a wavepacket.

The nuclear and electronic TDSEs are obtained by adding and subtracting a complex time-dependent potential energy surface (TDPES) $V_d(q, t)$ to the TDSE on the molecular wavefunction which separate as follows:

$$\hat{K}_q\psi + V_d(q, t)\psi = i\frac{\partial\psi}{\partial t}, \quad (7)$$

$$\hat{H}^{BO}\Phi + (\hat{D}^{(2)} + \hat{D}^{(1)})\Phi + \hat{V}^{ext}\Phi - V_d(q, t)\Phi = i\frac{\partial\Phi}{\partial t}. \quad (8)$$

The nuclear hamiltonian in Eq. (7), composed of the nuclear kinetic energy, \hat{K}_q and the so-far unspecified complex TDPES, V_d ,

$$V_d(q, t) := V_r(q, t) + iV_i(q, t), \quad (9)$$

does not include any explicit electron-nuclear coupling terms. The electronic TDSE (8) includes the Born-Oppenheimer BO Hamiltonian, \hat{H}^{BO} , of Eq. (2), consisting of the electronic kinetic energy and all Coulomb interactions, and if present, the external field \hat{V}^{ext} . This TDSE also includes the coupling terms, $\hat{D}^{(1)}$ and $\hat{D}^{(2)}$, containing the derivatives of Φ with respect to the nuclear coordinate,

$$\hat{D}^{(1)} := -\frac{\nabla_q\psi}{\psi}\frac{\nabla_q}{M}, \quad (10)$$

$$\hat{D}^{(2)} := -\frac{\nabla_q^2}{2M}. \quad (11)$$

The derivative coupling operator, $\hat{D}^{(1)}$, involves the log-derivative of ψ , $\nabla_q\psi/\psi$, presenting challenges for the numerical implementation of the XF equations. For future reference, let

us define this log-derivative through the nonclassical (r_ψ) and classical (p_ψ) components of the *nuclear momentum operator* applied to the nuclear function,

$$r_\psi(q, t) := \Re(\psi^{-1} \nabla_q \psi) = \frac{\nabla_q |\psi|}{|\psi|}, \quad (12)$$

$$p_\psi(q, t) := \Im(\psi^{-1} \nabla_q \psi) = \nabla_q(\arg \psi). \quad (13)$$

and define their counterparts for the electronic wavefunction,

$$r_\Phi(\mathbf{R}, q, t) := \Re(\Phi^{-1} \nabla_q \Phi) = \frac{\nabla_q |\Phi|}{|\Phi|}, \quad (14)$$

$$p_\Phi(\mathbf{R}, q, t) := \Im(\Phi^{-1} \nabla_q \Phi) = \nabla_q(\arg \Phi). \quad (15)$$

Now let us turn to the TDPES, or the nuclear potential defined in Eq. (9), which governs the dynamics of $\psi(q, t)$, and thus the factorization of $\Psi(\mathbf{R}, q, t)$. The choice of V_r should minimize the average residual nuclear momentum in Φ ,

$$\overline{p_\Phi} := \langle \Phi | p_\Phi | \Phi \rangle_{\mathbf{R}}, \quad (16)$$

while the role of V_i is to maintain the partial normalization condition, Eq. (6). As shown in Ref. [24] the norm-conserving V_i is equal to

$$V_i(q, t) = -\frac{1}{M} (2r_\psi + \nabla_q) \overline{p_\Phi}, \quad (17)$$

and there is a condition on the 'ideal' V_r , i.e. such V_r that $\overline{p_\Phi} = 0$,

$$\nabla_q V_r(q, t) = \langle \Phi | \nabla_q (\hat{H}_{BO} + \hat{V}^{ext}) | \Phi \rangle_{\mathbf{R}} + (4r_\psi + 2\nabla_q) \langle \Phi | \hat{D}^{(2)} | \Phi \rangle_{\mathbf{R}}. \quad (18)$$

If this condition is fulfilled, then $\overline{p_\Phi} = 0$ and $V_i \equiv 0$. While in one nuclear dimension V_r can be reconstructed (up to a time-dependent constant) from $\nabla_q V_r$ of Eq. (18), this is not the case for the coupled nuclear motion in many dimension. The ambiguity in the choice of V_r is related to the ambiguity of separating the full molecular phase between the nuclear and electronic components. Some choices of V_r are discussed in Ref. [24].

The imaginary potential V_i of Eq. (17) is exact if Φ is described in a complete basis. To maintain normalization of Φ in a finite basis used in this work, we introduce the following definition of V_i ,

$$V_i = \Im(\langle \Phi | \hat{H}_{el} | \Phi \rangle_{\mathbf{R}}), \quad (19)$$

compatible with the hermiticity of the full electronic hamiltonian,

$$\hat{H}_{el} = \hat{H}_{BO} + \hat{D}^{(1)} + \hat{D}^{(2)} + \hat{V}^{ext}, \quad (20)$$

once it is expressed in the matrix form. Both definitions of V_i conserve the trajectory weights and become equivalent in the complete basis limit.

The real potential V_r , which is the effective nuclear potential driving the time-evolution of the nuclear wavefunction ψ , also needs to be modified from Eq. 18 to account for finite electronic basis. We use a convenient definition similar to Eq. (19):

$$V_r = \Re(\langle \Phi | \hat{H}_{el} | \Phi \rangle_{\mathbf{R}}). \quad (21)$$

While not strictly minimizing $\overline{p_\Phi}$, this is essentially a mean-field potential associated with \hat{H}_{el} , the latter comprised of the Born-Oppenheimer hamiltonian, external field, and electron-nuclear coupling. Examples of other choices of V_r can be found in Ref. [24]; construction of optimal V_r for general systems is deferred to future work.

C. Quantum trajectory (QT) formalism

The de Broglie-Bohm-Madelung, often referred to as 'Bohmian', formulation of quantum mechanics [54, 55] provides an alternative to conventional basis/grid representations of multidimensional nuclear wavefunctions by recasting the TDSE into the trajectory framework. This is conceptually appealing because of an intuitive connection to classical molecular mechanics, widely used to study high-dimensional molecular systems. A review of the QT field is beyond the scope of this paper, but let us mention that the QTs were used to simulate single-surface and nonadiabatic dynamics [56–62], as well as to interpret the quantum phenomena [63, 64]. The Bohmian framework also served as a starting point for approximate and semiclassical methods, e.g. linearized quantum force [65], quantized Hamiltonian dynamics [66, 67], the QT-guided adaptable gaussian bases [68], and for the QT surface-hopping methods with and without the XF of molecular wavefunctions [31, 69, 70].

Within the Bohmian formulation a wavefunction is represented as an ensemble of quantum trajectories (QTs), evolving in time according to the classical-like equations of motion. The time-evolution of the probability density obeys the continuity equation. All the 'quantumness' comes from the non-local quantum potential added to the external 'classical' potential. In this section the formalism is outlined using the notations consistent with the rest of the paper, namely: one-dimensional coordinate q , the particle mass M and an external, possibly time-dependent, potential $V(q)$. A generalization to many dimensions and non-Cartesian coordinates is given, for example, in Ref. [71].

The Bohmian equations of motion follow from the polar representation of a complex wavefunction, $\psi(q, t)$, in terms of its real phase, $s(q, t)$, and amplitude, $|\psi(q, t)|$,

$$\psi(q, t) := |\psi(q, t)| e^{is(q, t)}, \quad (22)$$

substituted into the TDSE. We will use subscript t to indicate *quantities associated with the QT* at a position q_t , as opposed to *functions of q* . The gradient of the wavefunction phase, $p(q, t) = \nabla_q s(q, t)$, evaluated at the QT position q_t defines the QT momentum,

$$p_t = p(q, t)|_{q=q_t}, \quad (23)$$

which determines the dynamics of q_t according to the classical equation of motion (EOM),

$$\frac{dq_t}{dt} = \frac{p_t}{M}. \quad (24)$$

The trajectory velocity, p_t/M , defines the Lagrangian frame of reference,

$$\frac{d}{dt} := \frac{\partial}{\partial t} + \frac{p_t}{M} \nabla_q. \quad (25)$$

In this QT-frame of reference the EOMs following from the TDSE are:

$$\frac{dp_t}{dt} = -\nabla_q(V + U)|_{q=q_t} \quad (26)$$

$$\frac{ds_t}{dt} = \frac{p_t^2}{2M} - (V + U)|_{q=q_t}, \quad (27)$$

$$\frac{d\rho_t}{dt} = -\frac{\rho_t}{M} (\nabla_q p)|_{q=q_t}, \quad (28)$$

where $\rho_t = |\psi(q_t)|^2$ is the probability density and $U(q, t)$ is the quantum potential,

$$U(q, t) := -\frac{\hbar^2}{2M} \frac{\nabla_q^2 |\psi|}{|\psi|}. \quad (29)$$

The latter is \hbar^2/M (\hbar is included here explicitly) function which includes exactly the NQEs into otherwise classical Eqs (24-27).

A notable property of the QT dynamics is conservation of the trajectory weight, w_t ,

$$w_t := w(q_t) = |\psi(q_t)|^2 dq_t, \quad (30)$$

defined as the probability density within the volume element dq_t associated with a trajectory, q_t . As follows from the QT equations and Eq. (28) [72], w_t is constant in time,

$$w_t = w_0 = w,$$

allowing one to compute the expectation values of position-dependent and some momentum-dependent operators,

$$\langle \hat{O} \rangle_t = \int O(q) |\psi(q, t)|^2 dq \approx \sum_{i=1}^{N_{traj}} O(q_t^{(i)}) w^{(i)}, \quad (31)$$

without explicit construction of $\psi(q, t)$. In other words, upon the initial discretization of $\psi(q, 0)$ in terms of QTs and the associated weights, $\langle \hat{O} \rangle_t$ can be evaluated as a simple weighted sum over the trajectories at any time t . Equation (31) is used in this work when appropriate.

D. Equations of motion

Here we define the EOMs for the QTs evolving according to the FENDy formalism and for the electronic expansion coefficients, given the expansion of $\Phi(\mathbf{R}, q, t)$ in a stationary electronic basis, $\{\phi(\mathbf{R}, q)\}$,

$$\Phi(\mathbf{R}, q, t) := \sum_{\mu=1}^{N_{bas}} C_{\mu}(q, t) \phi_{\mu}(\mathbf{R}, q). \quad (32)$$

Index μ enumerates the functions in the basis $\{\phi\}$ of the size N_{bas} .

In FENDy, the nuclear trajectory momentum is defined by the *total* nuclear momentum:

$$p_t := p_{\psi} + \overline{p_{\Phi}}, \quad (33)$$

which includes the residual nuclear momentum of the electronic wavefunction, $\overline{p_{\Phi}}$ (Eq. (16)). Thus, the EOM for the nuclear wavefunction momentum is modified accordingly by the addition of a Lagrangian term proportional to $\overline{p_{\Phi}}/M$:

$$\frac{dp_{\psi}}{dt} = -\nabla_q (V_r + U)|_{q=q_t} + \frac{\overline{p_{\Phi}}}{M} \nabla_q p_{\psi}. \quad (34)$$

In the numerical implementation we use an equivalent to Eq. (29) representation of U in terms of r_ψ ,

$$U(q, t) := -\frac{r_\psi^2 + \nabla_q r_\psi}{2M}. \quad (35)$$

The trajectory positions evolve according to the total nuclear velocity p_t/M (Eq. (33)) as $dq_t/dt = p_t/M$. The trajectory weights are conserved due to the imaginary potential, V_i , as proved in Ref. [24]. The non-classical momentum itself is evaluated on the fly from the distribution of the trajectories and their weights as described in the next section.

The time evolution for the electronic basis coefficients, obtained from Eq. (32) and Eq. (8) in the moving frame, is governed by the following EOM,

$$\frac{d\mathbf{C}(q, t)}{dt} = -i\mathbf{S}^{-1}\mathbf{H}_D\mathbf{C} + \frac{p_t}{M}\nabla_q\mathbf{C}. \quad (36)$$

In Eq. (36) \mathbf{H}_D denotes the full electronic hamiltonian \hat{H}_{el} in the matrix form with subtraction of V_d ,

$$\mathbf{H}_D = \mathbf{H}^{BO} + \mathbf{V}^{ext} - \frac{\nabla_q\psi}{\psi}\frac{1}{M}(\mathbf{D}^{(1)} + \mathbf{S}\nabla_q) - \frac{1}{2M}(\mathbf{D}^{(2)} + \mathbf{S}\nabla_q^2 + 2\mathbf{D}^{(1)}\nabla_q) - \mathbf{S}V_d, \quad (37)$$

with the following matrix elements, where $(\mu, \lambda) = [1, N_{bas}]$:

$$S_{\mu\nu} = \langle \phi_\mu | \phi_\lambda \rangle_{\mathbf{R}}, \quad (38)$$

$$H_{\mu\nu}^{BO} = \langle \phi_\mu | \hat{H}^{BO} \phi_\lambda \rangle_{\mathbf{R}}, \quad (39)$$

$$V_{\mu\nu}^{ext} = \langle \phi_\mu | \hat{V}^{ext} \phi_\lambda \rangle_{\mathbf{R}}, \quad (40)$$

$$D_{\mu\nu}^{(1)} = \langle \phi_\mu | \nabla_q \phi_\lambda \rangle_{\mathbf{R}}, \quad (41)$$

$$D_{\mu\nu}^{(2)} = \langle \phi_\mu | \nabla_q^2 \phi_\lambda \rangle_{\mathbf{R}}. \quad (42)$$

In Section III the vectors $\mathbf{C}(q, t)$, defined for each trajectory q_t , will be listed together as columns of the matrix \mathbf{C} , its size being $N_{bas} \times N_{traj}$.

E. Basis set projection within the QT framework

Following Ref. [65] the necessary for the dynamics derivatives of functions, known at the trajectory positions, such as expansion coefficients \mathbf{C} and nuclear momenta p_ψ , are computed from their projections on a basis $\mathbf{f} = (f_1(q), f_2(q), \dots, f_N(q))$ of the size N . Let $F(q)$ and $\tilde{F}(q)$ denote a function/property and its expansion in a basis, respectively. Using $\mathbf{b} = (b_1, b_2, \dots, b_N)$ as a vector of the expansion coefficients, $\tilde{F}(q)$ is given by

$$\tilde{F}(q) = \sum_{k=1}^N b_k f_k(q) = \mathbf{f} \cdot \mathbf{b}. \quad (43)$$

The derivatives of $F(q)$ are then approximated by analytic derivatives of Eq. (43). As the basis functions are analytic, this approach is useful for differentiation on an unstructured grid and as a low-pass filter suppressing noise associated with the grid sparsity.

For the quantities required to solve the nuclear TDSE (7), the expansion coefficients \mathbf{b} are determined from the Least Squares Fit (LSF) weighted by the nuclear density [65]. Taking

advantage of the QT weight conservation (Eq. (31)), the LSF is determined by minimizing I evaluated as a weighted sum over trajectories,

$$I = \langle \psi(q) | (F(q) - \tilde{F}(q))^2 | \psi(q) \rangle \approx \sum_i^{N_{traj}} \left(F(q_t^{(i)}) - \tilde{F}(q_t^{(i)}) \right)^2 w^{(i)}. \quad (44)$$

Minimization of I with respect to the elements of \mathbf{b} gives their optimal values as solutions to the linear matrix equation,

$$\Omega \mathbf{b} = \mathbf{d}. \quad (45)$$

Here Ω is the overlap matrix of the basis functions and \mathbf{d} is the vector of projections with the elements,

$$\Omega_{kk'} = \sum_i^{N_{traj}} f_k(q_t^{(i)}) f_{k'}(q_t^{(i)}) w^{(i)}, \quad (46)$$

$$d_k = \sum_i^{N_{traj}} F(q_t^{(i)}) f_k(q_t^{(i)}) w^{(i)}. \quad (47)$$

Equation (45) is solved directly for \mathbf{b} , which defines $\tilde{F}(q)$ used to compute the necessary derivatives.

For the quantities in the electronic TDSE (8) – the coupling terms $\hat{D}^{(1)}$ and $\hat{D}^{(2)}$ and the residual nuclear momentum \bar{p}_Φ – we need the derivatives of the XF expansion coefficients arranged as the matrix \mathbf{C} . These are evaluated by the same procedure as above (Eqs (44-47)) with exception of using *equal weights* in Eq. (44), i.e. $w_i = 1$ for $i = [1, N_{traj}]$. This gives a statistical LSF, rather than the one based on integration over the nuclear space. Excluding the nuclear density gives more accurate fitting of the elements of \mathbf{C} in the regions of low wavefunction probability, reducing the error propagation from the low to high molecular density regions in the course of dynamics.

III. COMPUTATIONAL ALGORITHMS AND IMPLEMENTATION

The FENDy approach described in Section II and the electronic structure basis sets are implemented in Maple [73]. In this section we provide an overview of the implementation summarized in Tables II and III. The three major blocks include

- (i): initialization of the simulation parameters, projection and electronic bases (Table II, steps 1-5);
- (ii): initialization of the wavefunction, trajectories and electronic matrix elements (Table II, steps 6-8);
- (iii): time-integration (Table III, steps (9-23)).

The projection basis sets for the nuclei quantities are preset as follows:

- the nuclear momentum basis is $\mathbf{f}^{p_\psi} = \{1, e^{-3q}, \text{erf}(q/10)\}$;
- the non-classical momentum basis is $\mathbf{f}^{r_\psi} = \{1, q, e^{-3q}\}$;

FENDy algorithm
/Initialize basis sets/
1: Initialize standard electronic structure basis set
/Read Parameters/
2: QT parameters: Number of quantum trajectories and span
3: Electronic projection basis parameters: Number of Fourier functions and carrier frequency
4: Laser parameters: Width, peak time, intensity and frequency of the laser (Table I)
/Initialize auxiliary bases/
5: Define arrays for projections of p_ψ, r_ψ, V_d , and \mathbf{C}
/Initialize trajectories and electronic wavepackets/
6: Compute electronic matrix elements in AO basis
7: Initialize trajectories on a uniform grid
8: Initialize interpolation scheme for electronic matrix elements
/Time loop/

TABLE II. Steps of the numerical implementation of FENDy with complex potential. The time loop is described in Table III. The auxiliary basis sets with the exception of the Fourier basis are pre-defined. The electronic matrices (Eqs (38-42)) are pre-computed on a grid in q and are interpolated during the propagation.

– the basis for V_d (Eq. (9)) is $\mathbf{f}^{V_d} = \{1, e^{-11q/20}, e^{-11q/10}, 1/q\}$.

In block **(i)** the basis \mathbf{f}^{r_ψ} is chosen according to the analysis of the QT evolution of a wavepacket in the Morse potential [74]. The basis \mathbf{f}^{p_ψ} is chosen to describe a constant momentum for $q \rightarrow \infty$ with the parameters approximating the split-operator result, while the basis \mathbf{f}^{V_d} is determined by the fitting of the ground and excited Born-Oppenheimer surfaces. The electronic expansion coefficients \mathbf{C} (Eq. (32)) are projected on the Fourier basis of N_p sine and N_p cosine functions with a carrier frequency of $\pi/2$, plus a constant, resulting in a total basis of $N = 2N_p + 1$ functions. The electronic basis $\{\phi\}$ is defined either as the standard electronic structure basis set such as 6-31G, henceforth referred to as "*atomic orbital basis*" (AO), or as the eigenfunctions of \mathbf{H}^{BO} henceforth referred to as "*eigenbasis*". In block **(ii)** for computational efficiency the electronic matrix elements (Eqs (38-42)) are pre-computed on a grid in q . For the dynamics in the eigenbasis representation, \mathbf{H}^{BO} is diagonalized and the coupling matrices are computed in the eigenbasis. During the dynamics the pre-computed matrices are interpolated for any q using four-point Lagrange scheme. Details of the interpolation are described in Appendix A.

The time integration of block **(iii)** is performed via a self consistent loop comprised of steps 9-20 in Table III, modeled after Ref. [9]. Essentially, the time derivatives of all functions $F(t)$ – the trajectory positions $\{q_t\}$, momenta $\{p_t\}$, and electronic expansion coefficients \mathbf{C} – are evaluated using the average of their initial value $F(t)$ and value at the next step $F(t + dt)$ until consistency in $F(t + dt)$ is achieved. The error of the self-consistent loop is

Time propagation algorithm

*/**Time loop***/

for n from 1 to N_{steps} do

 */**Self-consistent propagation***/

 do

 */**Compute time-derivatives***/

 9: Electronic matrix elements via interpolation

 10: Project \mathbf{C} into Fourier basis

 11: Compute $(\hat{D}^{(1)} + \hat{D}^{(2)})|\Phi\rangle$

 12: Compute \bar{p}_Φ

 13: Compute $\frac{d}{dt}\mathbf{C}, \langle\Phi|\mathbf{H}_D|\Phi\rangle_{\mathbf{R}}$

 14: Project V_d into \mathbf{f}^{V_d}

 15: Project p_ψ into \mathbf{f}^{p_ψ}

 16: Compute quantum force

 17: Compute $\frac{d}{dt}p_\psi$ and $\frac{d}{dt}q_t$

 18: Compute sum of squares change in $F(t + dt)$ from previous step

 19: Compute average of $F(t + dt)$ and $F(t)$

 20: Project r_ψ of average into \mathbf{f}^{r_ψ}

 until **error** < **threshold** or **iteration** > **max(iteration)**

 */**Low pass filter***/

 21: Project \mathbf{C} , replace with $\tilde{\mathbf{C}}$ and re-normalize.

 22: Project r_ψ and replace with \tilde{r}_ψ

 23: Project p_ψ and replace with \tilde{p}_ψ

 end do

TABLE III. The time loop with self-consistent propagation scheme (steps 9-20). The low pass filter (steps 21-23) is applied at the end of each time-step.

equal to

$$\text{error} = \sum_{i=1}^{N_{traj}} \left((q_t^{(i)})^2 + (p_t^{(i)})^2 + \sum_{\mu=1}^{N_{bas}} |C_{i\mu}|^2 \right).$$

The projection of \mathbf{C} is outlined in Section II E. The quantities required to update \mathbf{C} are computed in steps 11-13, using $\psi^{-1}\nabla_q\psi = r_\psi + ip_\psi$ in evaluation of $\hat{D}^{(1)}$. Step 12 is the computation of the residual nuclear momentum, which is equal to

$$\bar{p}_\Phi := -i\langle\Phi\nabla_q\Phi\rangle,$$

provided that Φ satisfies the partial normalization condition Eq. (6). Therefore, \bar{p}_Φ is computed directly from $\langle\Phi|\hat{D}^{(1)}\Phi\rangle_{\mathbf{R}}$. Since the low-pass filter replaces \mathbf{C} with its projected approximation, $\tilde{\mathbf{C}}$, to maintain the normalization condition, the enusing Φ is re-normalized. The re-normalization introduces certain errors and, ideally, a constrained fitting procedure which enforces normalization while keeping \mathbf{C} in a basis, is desirable. Such a procedure (not discussed here) is relatively straightforward for an orthonormal electronic basis. However, we found this approach to be computationally expensive and not worth the effort in this application.

$N_{traj} = 50$	$\rho_{min} = 10^{-8}$	$dt = 0.25$ a.u.	$\text{threshold} = 10^{-15}$	$\text{iterations} = 10$
$d_{\omega 0} = \pi/2$	$N_p = 12$	$\epsilon = 10^{-9}$	$\alpha_{coh} = 8.16$	$\langle q \rangle_0 = 2.004$

TABLE IV. The simulation parameters include number of trajectories (N_{traj}), nuclear density cut-off (ρ_{min}) for $q_0^{(i)}$, time-step (dt), self-consistent propagation convergence criterion **threshold** and **iterations**, carrier frequency ($d_{\omega 0}$) and the number of sine/cosine functions (N_p) for the Fourier basis, unless specified otherwise, and interpolation error tolerance (ϵ). The nuclear wavefunction $\psi(q, 0)$ is specified by the width α_{coh} and center $\langle q \rangle_0$.

The projections of V_d and p_ψ (steps 14, 15 and 22) follow the procedure in Section II E using their respective bases. In step 16 the quantum force is computed from $\nabla_q U$ of Eq. (35), necessary to update the QT momenta (along with the QT positions) in step 17. In the LSF procedure (Eq. (45)) for r_ψ , the division by $|\psi(q, t)|$ is avoided by using integration by parts [75] when computing \mathbf{d} ,

$$d_k = -\frac{1}{2} \langle \psi | \nabla_q f_k | \psi \rangle_q = -\frac{1}{2} \sum_i^{N_{traj}} w^{(i)} \nabla_q f_k|_{q=q_t^{(i)}}. \quad (48)$$

Once the self-consistency error is below the threshold (or maximum number of iterations is reached), \mathbf{C} , p_ψ and r_ψ are projected on their respective bases once more in steps 21-23. This "low pass filter" is performed, i.e. these quantities are replaced with their fitted counterparts, to mitigate the high-frequency 'noise' acquired during the approximate propagation. The accuracy of the dynamics is achieved by increasing the Fourier basis (and improving the projection bases for p_ψ and r_ψ) at the cost of smaller time-step and/or more iterations in the self-consistent cycle.

IV. RESULTS AND DISCUSSION

The results discussed below are obtained for the 6-31G electronic basis set. Its functions act as the basis functions ϕ_μ of Eq. (32) when the formalism is implemented in the AO basis. For the eigenbasis implementation, ϕ_μ are defined as the eigenfunctions of \mathbf{H}^{BO} evaluated in the 6-31G AO basis. Unless noted otherwise, we discuss the results computed in the eigenbasis. The performance of FENDy is compared to the dynamics of the nuclear wavefunction propagated in time employing the conventional split-operator/Fast-Fourier Transform on a grid [76, 77]. In the eigenbasis implementation the couplings beyond the ground and first excited electronic states were found to be very small and, thus, they are set to zero to speed up the calculations and to facilitate comparison with the split-operator dynamics obtained for the same two-state nonadiabatic Hamiltonian in the presence of the laser field, V^{ext} . The split-operator results are referred to 'exact' throughout this section. The initial nuclear wavefunction is taken as a gaussian,

$$\psi(q, 0) = \left(\frac{\alpha_{coh}}{\pi} \right)^{1/4} \exp \left(-\frac{\alpha_{coh}}{2} (q - \langle q \rangle_0)^2 \right), \quad (49)$$

matching the ground state of the harmonic approximation to the ground BO surface at the minimum computed in the STO-3G basis. The ground electronic states is the only state

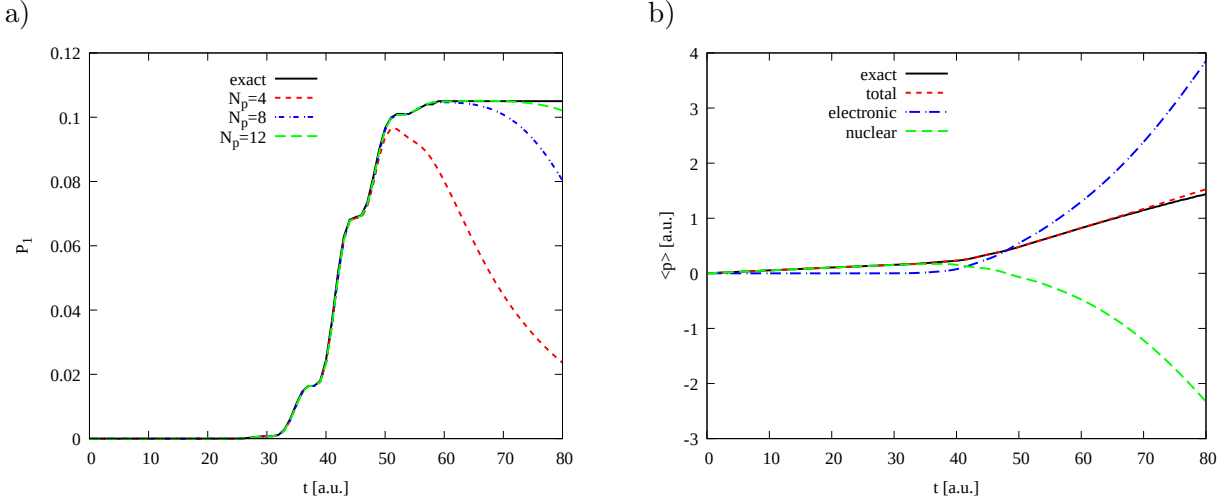


FIG. 1. (a) The excited state populations, P_1 , obtained with FENDy for $N_p = [4, 8, 12]$, shown as red dash, blue dot-dash and green long dash, respectively, compared to the exact result (black solid line) as functions of time t . (b) The total nuclear momentum for the molecular wavefunction Ψ ($\langle p \rangle = \langle \Psi | \hat{p} | \Psi \rangle$) and its electronic ($\langle \psi | \hat{p}_\phi | \psi \rangle_q$) and nuclear ($\langle \psi | p_\psi | \psi \rangle_q$) components, shown as red dash, blue dot-dash and green long dash, respectively, as functions of time t . The total momentum $\langle p \rangle$ from the exact dynamics is represented as black solid line.

populated at time $t = 0$. The results are presented for the dynamics parameters listed in Table IV unless noted otherwise.

First of all let us examine how FENDy captures the population dynamics. Figure 1(a) shows the population of the excited electronic state, which was initially unoccupied, for several values of the Fourier basis, $N_p = \{4, 8, 12\}$, used for the electronic coefficients \mathbf{C} . The population P_1 is defined as average of the nuclear density weighted by the electronic excited state populations. The population builds up with the increase of the laser intensity, which peaks at $t_0 = 40$ a.u., in 'waves' corresponding to the laser frequency. The FENDy results approach the exact results (black solid line) with the increase of the Fourier basis size. The population 'loss' at $t > 50$ a.u., i.e. the drop-off of the population instead of reaching a plateau once the laser pulse is turned off, is attributed to the re-projection of \mathbf{C} into the basis at the 'low pass filter' block (steps 21-23 in Table III). This trend is mitigated by increasing N_p . Once the laser intensity starts decreasing, the molecular wavefunction exhibits dissociative behavior as can be inferred from the average nuclear momentum, $\langle p \rangle$, displayed in Fig. 1(b). This quantity grows slowly from its initial value of zero up to t_0 and then exhibits notable increase, which reflects the dissociative motion on the purely repulsive excited PES, once its population becomes appreciable reaching about 10%.

The overall dynamics of the nuclear wavefunction $\psi(q, t)$, however, is dominated by the population of the ground electronic state. Within the QT representation of $\psi(q, t)$ this is seen in the evolution of the trajectory ensemble displayed in Fig. 2(a). The snapshots of the amplitudes of the ground state nuclear wavefunction, $|\psi_0(q, t)|$, from the conventional two-state nonadiabatic dynamics ('exact' split-operator calculations) are shown in Fig. 2(b) as functions of q on the vertical log-scale. The initially gaussian wavepacket is pulling away from the repulsive wall (small q), which is seen as compression of the QTs and squeezing of $|\psi_0(q, t)|$ with time for $q < 1.5$ a.u. This compression of QTs is the cause of the numerical 'noise', managed in our simulation by the low-pass filter, due to unphysical crossing of the

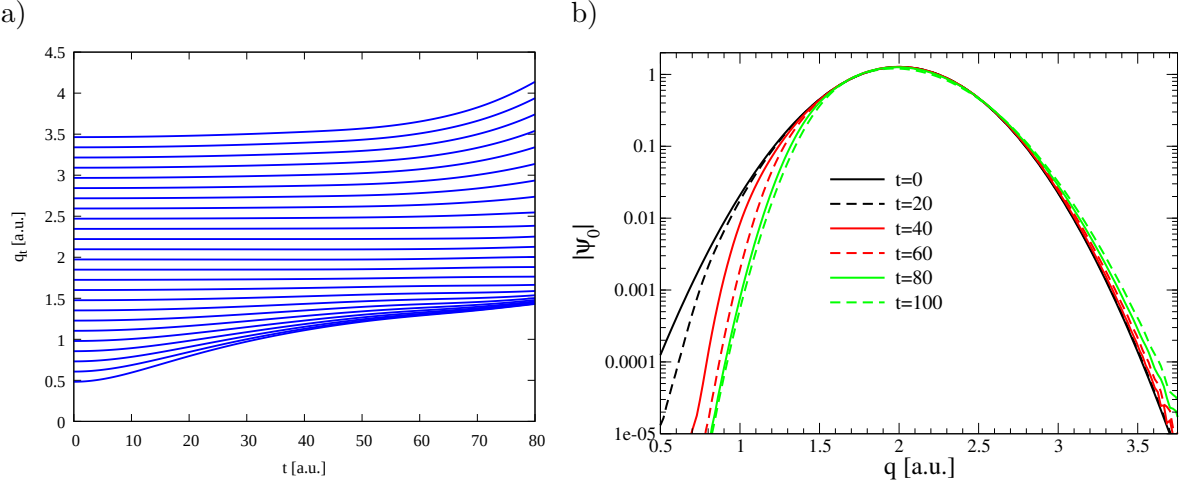


FIG. 2. Time-evolution of the nuclear wavefunction. (a) Positions $\{q_t\}$ of the quantum trajectory ensemble representing the nuclear wavefunction $\psi(q, t)$ within the XF representation as functions of time. Every other trajectory is shown for clarity. (b) The 'exact' ground state amplitudes, $|\psi_0(q, t)|$, as functions of the nuclear coordinate q , obtained from the conventional two-state nonadiabatic dynamics at times indicated in the legend.

trajectories resulting in the 'noisy' behavior of wavefunction properties computed at the QT positions, such as **C**. Focusing now on the right side of $|\psi_0(q, t)|$ we observe only small changes, i.e. the probability density in the ground state is largely stationary, despite the loss of the probability to the excited state. Within the XF, however, the nuclear wavefunction $\psi(q, t)$ represents the 'collective' dynamics on both ground and excited BO surfaces, which is seen in the dissociative behavior of QTs for $q > 2.5$ a.u. as time progresses.

Closer examination of the dynamics on the two BO surfaces, illustrated in Fig. 3, reveals that the dissociative dynamics begins after the laser intensity peaks, i.e. for $t > t_0$. The population on the excited state (blue line) is effectively 'held in place' by the laser pulse during the build up of its population. This is seen as the oscillatory behavior of the average nuclear position, $\langle q \rangle$, on the excited state for $t < 45$ a.u. and then increases as the nuclear wavepacket starts to dissociate (blue line in Fig. 3(a)). The average nuclear position on the ground state (red dash) remains essentially unchanged for the time interval shown in the figure. The population of the excited state and the laser pulse as functions of time are shown in Figs 3(b,c), respectively, to highlight the correlation between the population transfer and the laser pulse. The nuclear wavefunction bifurcation associated with the dissociative dynamics presents a major conceptual challenge to the XF formulation in general. Within our implementation it is manifested in the singularities in **C**, which make the numerical simulation crash, and limit the propagation time to essentially the early times of bifurcation. This issue is discussed below and at length in Ref. [41].

Now let us turn to the 'unique' feature of FENDy, i.e. the effective potential, $V_d(q, t)$, driving the dynamics of the nuclear wavefunction, defined here as the expectation value of the electronic hamiltonian and coupling terms, Eq. (20). As a reminder, V_d , is a time-dependent complex function of the nuclear coordinate, with its real part, V_r , acting as the time-dependent PES on which $\psi(q, t)$ evolves, and its imaginary part, V_i , enforcing the normalization of the electronic wavefunction $\Phi(\mathbf{R}, q, t)$ for each q . The 'ideal' V_r means that the residual nuclear momentum, $\overline{p_\phi}$ of Eq. (16), in the electronic wavefunction and V_i

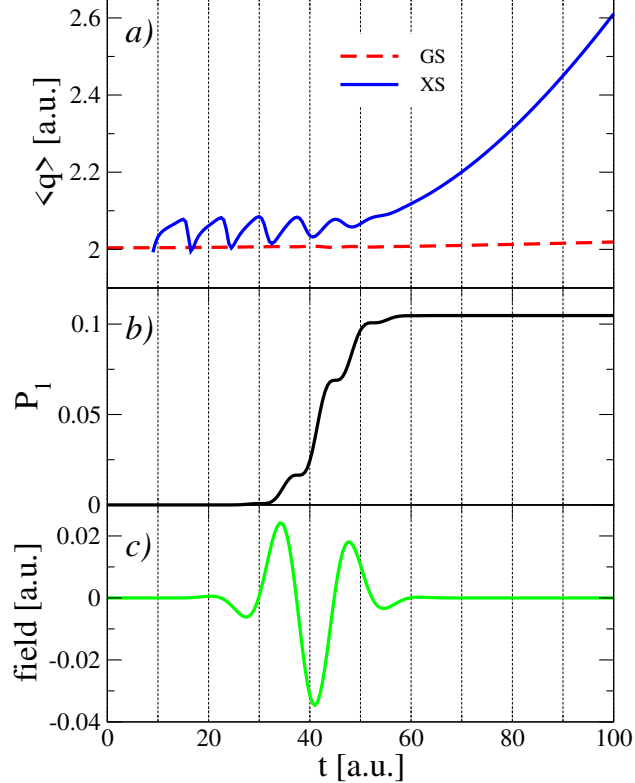


FIG. 3. Properties of the excited state dynamics (computed exactly): (a) average position of the ground (red dashed line) and excited (blue solid line) nuclear wavefunctions; (b) excited state population; (c) the electric field of the laser pulse.

are both equal to zero. We verified that in our model (one nuclear degree of freedom) as implemented, V_r is, indeed, 'ideal' in the *absence* of the laser pulse: since the H_2^+ system is characterized by a large energy gap between the ground and excited electronic states, V_r is essentially the same as the ground BO PES, $V_i = 0$ and $\bar{p}_\psi = 0$. However, with the laser pulse present, V_r exhibits features responsible for the dissociation of the nuclear wavefunction due to the electron-nuclear coupling as illustrated in Fig. 4(a). The BO surfaces are plotted alongside V_r snapshots for reference. Given our "mean-field" like definition of V_r , we also compared it to the Ehrenfest surfaces defined as,

$$V^{Erf} = \langle \Phi | \hat{H}^{BO} + \hat{V}^{ext} | \Phi \rangle_R,$$

at each trajectory and projected into the same basis as V_r (Fig. 4(b)). The difference between the two types of surface is in the electron-nuclear coupling due to the operators $\hat{D}^{(1)}$ and $\hat{D}^{(2)}$. For both types of surfaces in Fig. 4, we note the appearance of a "hill" in the region of $q = [2.0, 2.5]$ a.u. as the time progresses. This "hill" corresponds to the position of the bulk of electronic excitation within the nuclear subspace; the force from this surface would give nuclear trajectories at $q < 2$ a.u. the negative momentum as seen in Fig. 7. We find V_r to be nearly identical to the Ehrenfest surfaces at early times with the difference appearing at $t = 80$ a.u. These snapshots are plotted together in Fig. 5. The difference between the two is due to the larger electron-nuclear coupling at later times (also observed in the large $\langle \bar{p}_\phi \rangle_q$ in Fig. 1(b)), as the Ehrenfest surface neglects these terms. Despite its simplicity, the definition of V_r implemented in this work is clearly 'sub-optimal' as seen in

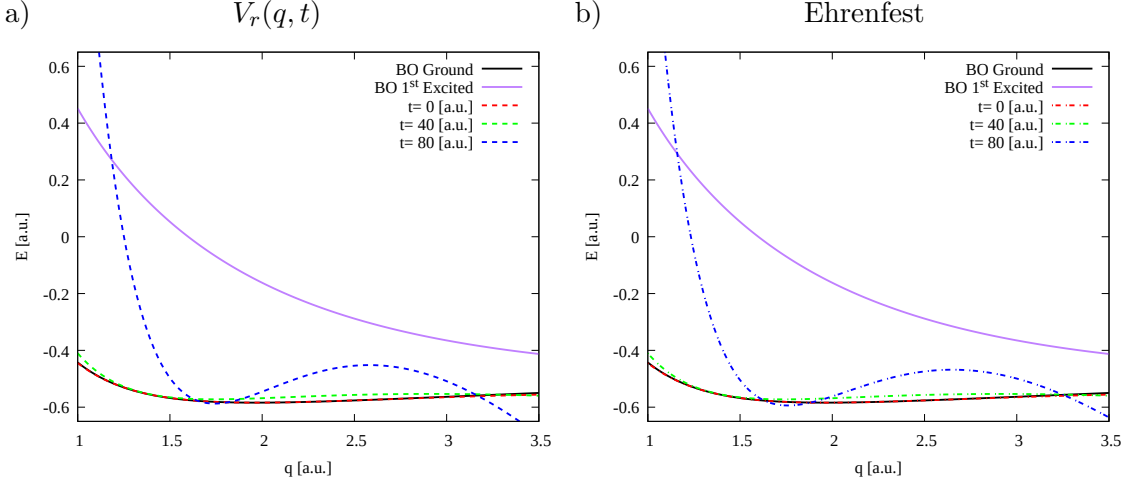


FIG. 4. Snapshots of (a) V_r (dashed lines) and (b) the Ehrenfest surfaces (dot dashed lines) projected into the basis. In both panels the solid lines are the ground (black) and excited (purple) BO surfaces. Note the appearance of a "hill" centered around $q = 2.5$ in both panels.

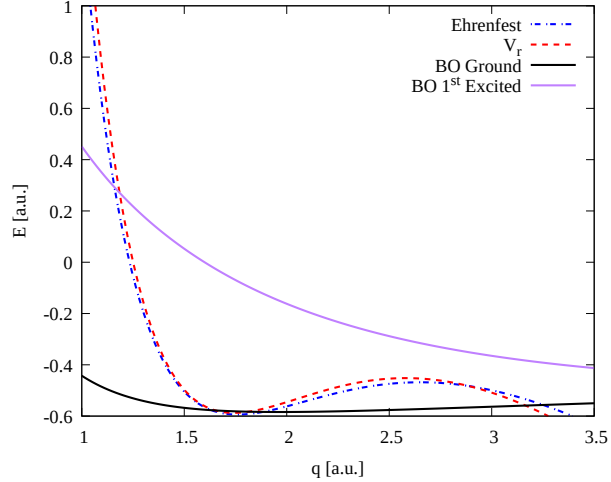


FIG. 5. The Ehrenfest surface (dot dash) and V_r (dashed) at $t = 80$ a.u. The BO surfaces are given for reference.

the large \overline{p}_ϕ it generates. This conclusion is consistent with our results for the vibrationally nonadiabatic model [24]. Alternative V_r , minimizing \overline{p}_ϕ , are considered in Ref. [24], and are currently under development in our group.

Now let us examine the computed $V_i(q, t)$ and $\overline{p}_\phi(q, t)$ in more detail. In our simulation $V_i(q, t)$, shown in Fig. 6(a), is very close to zero until the onset of the wavefunction bifurcation in the nuclear coordinate. This behavior is manifested in the dynamics of the nuclear momentum components, p_ψ , and $\langle \overline{p}_\phi \rangle_q$ (Fig. 6(b)), with the former decreasing and latter increasing after $t > 40$ a.u. The nuclear momentum components as functions of q are shown in Fig. 7 at $t = 60$ and $t = 80$ a.u. Note that in both instances near the equilibrium bond length of $q = 2$ a.u., which is the most populated region of the nuclear subspace, p_ψ is negative and \overline{p}_Φ is positive; they add up to the total nuclear momentum that is close

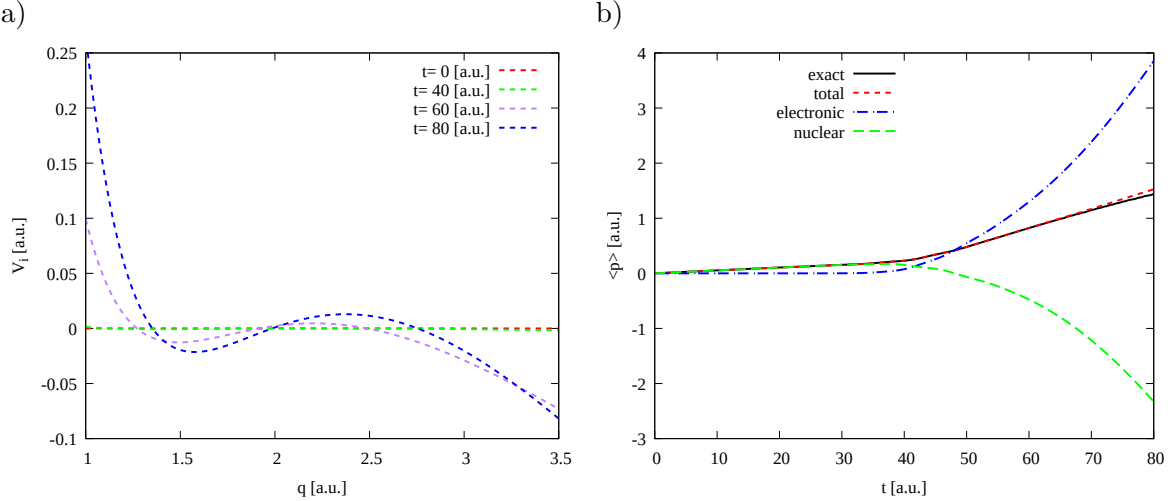


FIG. 6. (a) Snapshots of the imaginary part of the time-dependent potential as a function of q . (b) The nuclear momentum components averaged over the nuclear sub-space as functions of time (same as Fig. 1(b)).

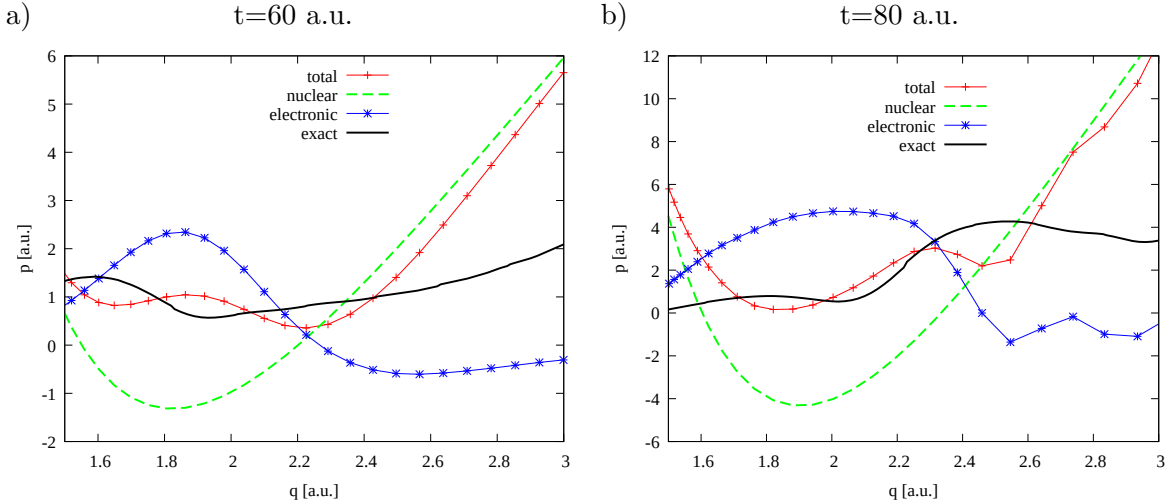


FIG. 7. The nuclear momentum components as functions of q for (a) $t = 60$ a.u. and (b) $t = 80$ a.u. In both panels: the black line represents the exact total nuclear momentum; the red curve is the total nuclear momentum in FENDy, the green dash is p_ψ and the blue curve is \bar{p}_Φ , with the dots marking the positions of the QTs.

to the split-operator result. Despite the discrepancies between the exact and FENDy nuclear momenta in Fig. 7, their averages are in reasonable agreement (Fig. 1(b)) given the nuclear density distribution. If the laser is turned off, then the computed \bar{p}_Φ remains zero (not shown), suggesting that in this model the residual nuclear momentum of the electronic wavefunction is introduced by the laser. Large values of \bar{p}_Φ correspond to a large imaginary potential which is consistent with Eq. (17). Without the laser pulse, the imaginary potential remains zero.

Next we will discuss the challenges of stable propagation of the electronic coefficients

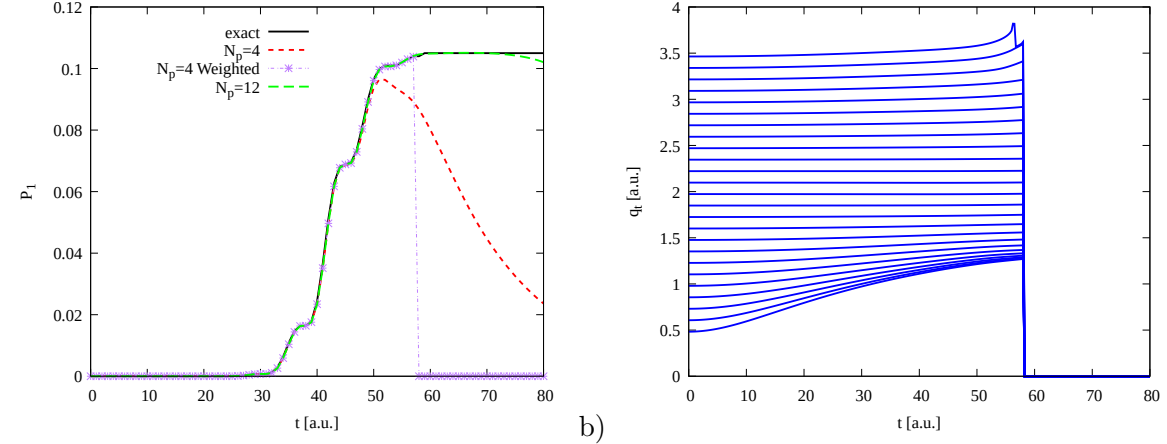


FIG. 8. Panel a: The same as Fig. 1a, except the purple line is computed using weighted fits of \mathbf{C} . Panel b: The same as Fig. 2a but computed with weighted fits. The simulation crashed around $t = 60$ a.u. due to accumulated noise in the electronic boundaries from the weighted fits.

C. One already mentioned challenge is the unphysical 'erratic' values of \mathbf{C} due to crossing of trajectories: the approximate quantum force does not fully balance the forces acting on the trajectories on the steep potential wall. This results in the interdispersed reflected and incoming subgroups of trajectories, each with different values of \mathbf{C} and p_ψ , and essentially random values of derivatives of these quantities. This artifact is mitigated with the low pass filter procedure described in Section III. Another significant challenge of numerical XF are the non-trivial electronic boundary conditions in q as consequence of the partial normalization condition, which must be maintained even in the regions of very low overall probability density. We demonstrate this by comparing the unweighted and weighted (with the nuclear density) fits of \mathbf{C} (described in Section II E). In Fig. 8(a), we present populations obtained with unweighted and weighted projections. As expected the weighted projections provide more accurate description of the nuclear-averaged behavior with a smaller Fourier basis, but instabilities in the tails of the density eventually crash the simulation. These instabilities are more apparent in Fig. 8(b) where the tail trajectories behave erratically as a result of significant errors in \bar{p}_ϕ . In principle, this can be resolved using analytic boundary conditions, which is non-trivial in the delocalized laser field. We mitigate the problem by fitting electronic coefficients independent of the nuclear density (i.e. 'unweighted fits'), improving the accuracy at the boundary regions at the cost of reduced accuracy in expectation values.

Finally, we illustrate the equivalence of the atomic basis and eigenbasis. Performing the dynamics directly in the atomic basis, without computing the eigenstates, is one of the attractive features of the XF electron-nuclear dynamics. The average nuclear momenta obtained in two FENDy implementations are displayed in Fig. 9. We see that not just the total nuclear momenta computed in the eigenbasis and directly in the atomic basis match, but p_ψ and $\langle \bar{p}_\phi \rangle$ are identical as well. The comparison of the orbital coefficients (Table V) reinforces this point. The same simulation is performed using the AO representation and we compare the two electronic wavefunctions obtained at $t = 21$ a.u. at the central (25th) trajectory by projecting the eigenbasis wavefunction back into the AO basis. As expected the AO coefficients show excellent agreement (better than 10^{-4}).

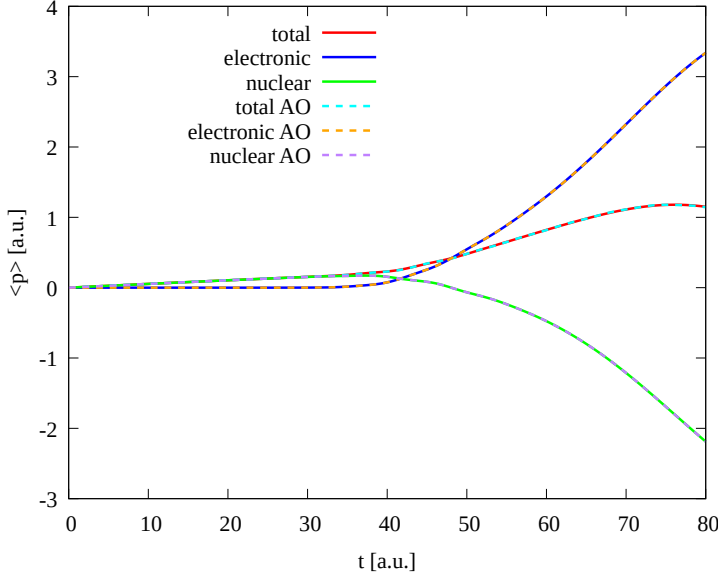


FIG. 9. The nuclear momentum components computed in the eigenbasis and AO basis with $N_p=8$. The eigenbasis/AO basis results are shown as with solid lines/dashes, respectively.

AO coefficient	AO simulation	eigenbasis simulation
H_{1s}^L	$-0.38251 - 0.00063i$	$-0.38259 - 0.00052i$
H_{2s}^L	$-0.25794 - 0.00115i$	$-0.25784 - 0.00111i$
H_{1s}^R	$-0.38168 + 0.00040i$	$-0.38169 + 0.00052i$
H_{2s}^R	$-0.25588 + 0.00108i$	$-0.25590 + 0.00111i$

TABLE V. Coefficients of 1s and 2s functions of 6-31G basis set on each atom (L, R) on the central trajectory at $t = 21$ a.u.

V. CONCLUSIONS

In this paper, we presented a successful numerical implementation of FENDy in a molecular model with real Coulomb interactions and an external field. We demonstrate that the FENDy code is able to reproduce the exact dynamics obtained in a two-state model using the split-operator method. Most importantly, the method is developed without referencing the electronic eigenstates, and we demonstrated that the same result is achieved without solving the electronic structure. The biggest challenge of implementing the numerical XF was identified as the non-local effects associated with the electronic coefficients \mathbf{C} . Beyond the challenges of working with an unstructured grid in the trajectory representation of the nuclear wavefunction – something specific to the nuclear dynamics methods employed in this work – we find the XF formalism itself presents significant numerical challenges when describing \mathbf{C} .

Firstly, the diverging nuclear wavepackets in the H_2^+ model (and many other photochemical systems) lead to singularities in \mathbf{C} due to the XF definition of the nuclear wavefunction, further explored in Ref. [41]. Secondly, the partial normalization condition leads to non-trivial electronic boundary conditions. In this work we showed that the improper treat-

ment of the electronic boundary (where the nuclear density is small) results in noise that propagates into the high density regions and crashes the calculation, and that the use of unweighted fitting procedure for \mathbf{C} alleviates this problem. The diverging nuclear dynamics may be less of a problem for larger systems in the regime of electronic wavepackets, which is the envisioned regime of FENDy, rather than a superposition of effectively only two states. We also note that the use of basis set projections for $\nabla_q \psi / \psi$, as in Ref. [78], eliminate this commonly cited (e.g. Refs [39, 40]) source of numerical difficulty for XF.

Specific for FENDy with complex effective nuclear potential V_d , we found the V_d derived for exact Φ led to errors in the finite basis representation. Thus we employed a simple definition of V_d , which is consistent with the finite basis representation and maintains the partial normalization condition. However, this definition results is not ideal as it leads to a large residual nuclear momentum of the electronic wavefunction. Better definitions of V_r , as well as the problem of diverging nuclear wavepackets and improved description of the electronic boundaries are the focus of the current and future investigation in our group.

ACKNOWLEDGEMENT

This material is based upon work supported by the National Science Foundation of U.S.A. under Grant No. CHE-2308922.

ADDITIONAL INFORMATION

Conflict of interests: The authors declare that they have no known competing financial interests or personal relationships that could have appeared to influence the work reported in this paper

Data availability: The code described in this work and used to generate the data is freely available on GitHub at: <https://github.com/julianps1/Factorized-electron-nuclear-dynamics/tree/main>

Appendix A: Interpolation Scheme

In principle the code is compatible with on-the-fly electronic structure calculations; however, for computational efficiency we use a four-point Lagrange interpolation [79] for electronic matrix elements. In the AO representation, this is done for \mathbf{H}^{BO} matrix elements. In the eigenbasis representation, this is done for all electronic matrix elements (except the overlap) as we do not have analytic expressions for the electronic eigenfunctions in q .

We find approximate analytic forms of the boundary $q \rightarrow \infty$ to avoid computing a large number of interpolation points for dissociating trajectories, by assuming the wavefunction approaching the non-interacting atomic limit at large $q > q_{cut}$. The cutoff, q_{cut} , is determined by the deviation of overlap matrix of the AOs below the preset tolerance, ϵ , Table IV. The energy and expansion coefficients are then:

$$F(q) := Ae^{-\alpha q} + F_{atomic} \text{ if } q > q_{cut}, \quad (\text{A1})$$

here F_{atomic} is the value of the energy or expansion coefficient of the given state in the atomic limit for the eigenbasis. In the AO basis, these are the elements of \mathbf{H}^{BO} in the atomic limit

and include an additional $-1/q$ term scaled by the overlap of the basis functions (computed in the atomic limit) for the given matrix element. The exponential function is used to smoothly connect the asymptotic value to the numeric result at the cutoff. The scaling parameter α is computed from a 3-point finite difference at the cutoff. For AOs this is computed from the largest overlap matrix element and for the eigenbasis it is computed from the energy. The parameter A is chosen such that the analytic value is equal to the numeric value at q_{cut} after obtaining α .

In the eigenbasis representation we define analytic boundaries for the $q = 0$ limit as the solutions become singular at $q = 0$. The cutoff is chosen as $q_{cut} = 0.5$ a.u. which gives reasonable accuracy in this model before the AOs become too degenerate. Here, the analytic form of the energy is chosen as

$$E(q) := aq^2 + E_0 \quad (A2)$$

where the quadratic parameter is defined such that the numeric and analytic solutions are equal at the cutoff, and E_0 is the energy at $q = 0$. For the coefficients we add a linear parameter:

$$C(q) := aq^2 + bq + C_0(q) \quad (A3)$$

where C_0 is the coefficient at $q = 0$. The linear and quadratic terms are determined such that the function value and first derivative are equal at the cutoff.

The analytic solutions at $q = 0$ are obtained by a non-unitary transformation to the degenerate pairs of basis functions ϕ :

$$\begin{aligned} g_\lambda &:= \frac{1}{2}\phi_\lambda^{(1)} + \frac{1}{2}\phi_\lambda^{(2)}, \\ u_\lambda &:= \frac{1}{\sqrt{2\sigma}q}\phi_\lambda^{(1)} - \frac{1}{\sqrt{2\sigma}q}\phi_\lambda^{(2)}, \end{aligned} \quad (A4)$$

where s_λ is a quadratic coefficient obtained from,

$$\langle \phi_\lambda^{(1)} | \phi_\lambda^{(2)} \rangle_{\mathbf{R}} = 1 - s_\lambda q^2, \quad (A5)$$

here the numeric superscript indexes the atom with greek indexing the basis function. With this transformation, the new overlap matrix is non-degenerate as the new basis functions are orthogonal by construction and the singularities are in the analytic transformation matrix. The analytic $\mathbf{D}^{(1)}$ and $\mathbf{D}^{(2)}$ matrix elements are obtained with a second order Taylor expansion at the cutoff to ensure they are smooth.

[1] Chad A. Mirkin, Sarah Hurst Petrosko, Natalie Artzi, Koray Aydin, Austin Biaggne, C. Jeffrey Brinker, Katherine E. Bujold, Y. Charles Cao, Rachel R. Chan, Chaojian Chen, Peng-Cheng Chen, Xiaodong Chen, Olivier J. G. L. Chevalier, Chung Hang Jonathan Choi, Richard M. Crooks, Vinayak P. Dravid, Jingshan S. Du, Sasha B. Ebrahimi, Hongyou Fan, Omar K. Farha, C. Adrian Figg, Tanner D. Fink, Connor M. Forsyth, Harald Fuchs, Franz M. Geiger, Nathan C. Gianneschi, Kyle J. Gibson, David S. Ginger, SiShi Guo, Justin S. Hanes, Lian-gliang Hao, Jin Huang, Bryan M. Hunter, Fengwei Huo, Jeongmin Hwang, Rongchao Jin, Shana O. Kelley, Thomas J. Kempa, Youngeun Kim, Sergej Kudruk, Sneha Kumari, Kaitlin M. Landy, Ki-Bum Lee, Noel J. Leon, Jun Li, Yuanwei Li, Zhiwei Li, Bin Liu, Guoliang Liu, Xiaogang Liu, Luis M. Liz-Marzán, Jochen H. Lorch, Taokun Luo, Robert J. Macfarlane, Jill E.

Millstone, Milan Mrksich, Catherine J. Murphy, Rajesh R. Naik, Andre E. Nel, Christopher Oetheimer, Jenny K. Hedlund Orbeck, So-Jung Park, Benjamin E. Partridge, Nicholas A. Pеппас, Michelle L. Personick, Arindam Raj, Namrata Ramani, Michael B. Ross, Stacey Barnaby Ross, Edward H. Sargent, Tanushri Sengupta, George C. Schatz, Dwight S. Seferos, Tamar Seideman, Soyoung Eileen Seo, Bo Shen, Wooyoung Shim, Donghoon Shin, Ulrich Simon, Andrew J. Sinegra, Peter T. Smith, Alexander M. Spokoyny, Peter J. Stang, Alexander H. Stegh, J. Fraser Stoddart, Dayne F. Swearer, Weihong Tan, Michelle H. Teplensky, C. Shad Thaxton, David R. Walt, Mary X. Wang, Zhe Wang, Wei David Wei, Paul S. Weiss, Peter H. Winegar, Younan Xia, Yi Xie, Xiaoyang Xu, Peidong Yang, Yiming Yang, Zihao Ye, Kuk Ro Yoon, Cuizheng Zhang, Hua Zhang, Ke Zhang, Liangfang Zhang, Xiaoyu Zhang, Ye Zhang, Zijian Zheng, Wenjie Zhou, Shengshuang Zhu, and Wei Zhu. 33 unresolved questions in nanoscience and nanotechnology. *ACS Nano*, 19(36):31933–31968, 2025. doi:10.1021/acsnano.5c12854.

- [2] Ding Xu, Arkajit Mandal, James M. Baxter, Shan-Wen Cheng, Inki Lee, Haowen Su, Song Liu, David R. Reichman, and Milan Delor. Ultrafast imaging of polariton propagation and interactions. *Nat. Commun.*, 14(1), Jun 30 2023. doi:10.1038/s41467-023-39550-x.
- [3] Jonathan D. Schultz, Jonathon L. Yuly, Eric A. Arsenault, Kelsey Parker, Sutirtha N. Chowdhury, Reshmi Dani, Sohang Kundu, Hanggai Nuomin, Zhendian Zhang, Jesús Valdiviezo, Peng Zhang, Kaydren Orcutt, Seogjoo J. Jang, Graham R. Fleming, Nancy Makri, Jennifer P. Ogilvie, Michael J. Therien, Michael R. Wasielewski, and David N. Beratan. Coherence in chemistry: Foundations and frontiers. *Chem. Rev.*, 124(21):11641–11766, 2024. doi:10.1021/acs.chemrev.3c00643.
- [4] B. Xiang and W. Xiong. Molecular polaritons for chemistry, photonics and quantum technologies. *Chem. Rev.*, 124(5):2512–2552, 2024. doi:10.1021/acs.chemrev.3c00662.
- [5] Lachlan P. Lindoy, Arkajit Mandal, and David R. Reichman. Quantum dynamical effects of vibrational strong coupling in chemical reactivity. *Nat. Commun.*, 14(1), May 12 2023. doi:10.1038/s41467-023-38368-x.
- [6] Rameshwar L. Kumawat and George C. Schatz. Density functional tight binding insights into plasmonic silver–platinum nanoparticles and alloys for enhanced photocatalysis. *ACS Appl. Nano Mater.*, 8(37):18042–18055, 2025. doi:10.1021/acs.anm.5c03232.
- [7] Lili Rassouli, Mohammad Shakiba, Alexey V. Akimov, Xuyan Ma, and Michel Dupuis. Excitons in hematite Fe_2O_3 : Short-time dynamics from TD-DFT and non-adiabatic dynamics theories. *J. Phys. Chem. C.*, 128(33):13681–13693, 2024. doi:10.1021/acs.jpcc.4c03247.
- [8] Sarah Pak, Muhammed A. Dada, Niranjan Govind, and Daniel R. Nascimento. Fast simulation of soft x-ray near-edge spectra using a relativistic state-interaction approach: Application to closed-shell transition metal complexes. *J. Chem. Phys.*, 163(9), September 2025. doi:10.1063/5.0276628.
- [9] Jacek Jakowski, Wenchang Lu, Emil Briggs, David Lingerfelt, Bobby G. Sumpter, Panchapakesan Ganesh, and Jerzy Bernholc. Simulation of 24,000 electron dynamics: Real-time time-dependent density functional theory (TDDFT) with the real-space multigrids (RMG). *J. Chem. Theory Comput.*, 21(3):1322–1339, 2025. doi:10.1021/acs.jctc.4c01241.
- [10] Thomas E. Markland and Michele Ceriotti. Nuclear quantum effects enter the mainstream. *Nat. Rev. Chem.*, 2:0109, 2018. doi:10.1038/s41570-017-0109.
- [11] Julien F. Rowen, Frederike Beyer, Tim Schleif, and Wolfram Sander. Isomer-specific heavy-atom tunneling in the ring expansion of fluorenylazirines. *J. Org. Chem.*, 88(13):7893–7900, 2023. doi:10.1021/acs.joc.3c00484.
- [12] John C. Light and Tucker Carrington Jr. *Discrete-Variable Representations and Their*

Utilization, pages 263–310. John Wiley & Sons, Ltd, 2000. ISBN 9780470141731. doi: <https://doi.org/10.1002/9780470141731.ch4>.

- [13] Apurba Nandi, Riccardo Conte, Priyanka Pandey, Paul L. Houston, Chen Qu, Qi Yu, and Joel M. Bowman. Quantum nature of ubiquitous vibrational features revealed for ethylene glycol. *J. Chem. Theory Comput.*, 21(10):5208–5220, 2025. doi:10.1021/acs.jctc.5c00173.
- [14] Xiao-Gang Wang and Tucker Carrington. Using an uncontracted inter-molecular basis to assess the convergence of contracted inter-molecular bases when computing the spectrum of H₂O-CO. *Mol. Phys.*, 0(0):e2466666, 2025. doi:10.1080/00268976.2025.2466666.
- [15] Peter M. Felker Minzhong Xu and Zlatko Baćić. Light molecules inside the nanocavities of fullerenes and clathrate hydrates: Inelastic neutron scattering spectra and the unexpected selection rule from rigorous quantum simulations. *Int. Rev. Phys. Chem.*, 39(4):425–463, 2020. doi:10.1080/0144235X.2020.1794097.
- [16] Peter M. Felker and Zlatko Baćić. HF trimer: 12D fully coupled quantum calculations of HF-stretch excited intramolecular and intermolecular vibrational states using contracted bases of intramolecular and intermolecular eigenstates. *J. Chem. Phys.*, 158(23):234109, 06 2023. doi:10.1063/5.0156976.
- [17] Irén Simkó, Peter M. Felker, and Zlatko Baćić. H₂O trimer: Rigorous 12D quantum calculations of intermolecular vibrational states, tunneling splittings, and low-frequency spectrum. *J. Chem. Phys.*, 162(3):034301, 01 2025. ISSN 0021-9606. doi:10.1063/5.0250018.
- [18] J. C. Tully. Chemical dynamics at metal surfaces. *Annu. Rev. Phys. Chem.*, 51(Volume 51, 2000):153–178, 2000. ISSN 1545-1593. doi: <https://doi.org/10.1146/annurev.physchem.51.1.153>.
- [19] A. Abedi, N. T. Maitra, and E. K. U. Gross. Exact factorization of the time-dependent electron-nuclear wave function. *Phys. Rev. Lett.*, 105:123002, Sep 2010. doi: 10.1103/PhysRevLett.105.123002.
- [20] N. M. Hoffman, H. Appel, A. Rubio, and N. T. Maitra. Light-matter interactions via the exact factorization approach. *Eur. Phys. J. B*, 91(180):14, 08 2018. doi: <https://doi.org/10.1140/epjb/e2018-90177-6>.
- [21] A. Abedi, E. Khosravi, and I. V. Tokatly. Shedding light on correlated electron–photon states using the exact factorization. *Eur. Phys. J. B*, 91(194):12, 08 2018. doi: <https://doi.org/10.1140/epjb/e2018-90243-1>.
- [22] E. Sangiogo Gil, D. Lauvergnat, and F. Agostini. Exact factorization of the photon–electron–nuclear wavefunction: Formulation and coupled-trajectory dynamics. *J. Chem. Phys.*, 161(8):084112, 08 2024. ISSN 0021-9606. doi:10.1063/5.0224779.
- [23] R. Martinazzo and I. Burghardt. Quantum dynamics with electronic friction. *Phys. Rev. Lett.*, 128:206002, May 2022. doi:10.1103/PhysRevLett.128.206002.
- [24] S. Garashchuk, J. Stetzler, and V. Rassolov. Factorized electron–nuclear dynamics with an effective complex potential. *J. Chem. Theory Comput.*, 19(5):1393–1408, 2023. doi: 10.1021/acs.jctc.2c01019.
- [25] S. K. Min, F. Agostini, and E. K. U. Gross. Coupled-trajectory quantum-classical approach to electronic decoherence in nonadiabatic processes. *Phys. Rev. Lett.*, 115:073001, Aug 2015. doi:10.1103/PhysRevLett.115.073001.
- [26] D. Han and A. V. Akimov. Nonadiabatic dynamics with exact factorization: Implementation and assessment. *J. Chem. Theory Comput.*, 20(12):5022–5042, 2024. doi: 10.1021/acs.jctc.4c00343.
- [27] B. F. E. Curchod, F. Agostini, and I. Tavernelli. CT-MQC - a coupled-trajectory mixed

quantum/classical method including nonadiabatic quantum coherence effects. *Eur. Phys. J. B*, 91(168):12, 07 2018. doi:10.1140/epjb/e2018-90149-x.

[28] S. K. Min, F. Agostini, I. Tavernelli, and E. K. U. Gross. Ab initio nonadiabatic dynamics with coupled trajectories: A rigorous approach to quantum (de)coherence. *J. Phys. Chem. Lett.*, 8(13):3048–3055, 2017. doi:10.1021/acs.jpclett.7b01249.

[29] L. M. Ibele, E. Sangiogo Gil, E. V. Arribas, and F. Agostini. Simulations of photoinduced processes with the exact factorization: State of the art and perspectives. *Phys. Chem. Chem. Phys.*, 26:26693–26718, 2024. doi:10.1039/D4CP02489C.

[30] Daeho Han and Alexey V. Akimov. Nonadiabatic dynamics with exact factorization: Implementation and assessment. *J. Chem. Theory Comput.*, 20(12):5022–5042, 2024. doi:10.1021/acs.jctc.4c00343.

[31] L. Dupuy, A. Rikus, and N. T. Maitra. Exact-factorization-based surface hopping without velocity adjustment. *J. Phys. Chem. Lett.*, 15(10):2643–2649, 2024. doi:10.1021/acs.jpclett.4c00115.

[32] Y. Suzuki, A. Abedi, N. T. Maitra, and E. K. U. Gross. Laser-induced electron localization in H_2^+ : Mixed quantum-classical dynamics based on the exact time-dependent potential energy surface. *Phys. Chem. Chem. Phys.*, 17:29271–29280, 2015. doi:10.1039/C5CP03418C.

[33] A. Abedi, N. T. Maitra, and E. K. U. Gross. Correlated electron-nuclear dynamics: Exact factorization of the molecular wavefunction. *J. Chem. Phys.*, 137(22), August 2012. ISSN 1089-7690. doi:10.1063/1.4745836.

[34] S. Shin and H. Metiu. Nonadiabatic effects on the charge transfer rate constant: A numerical study of a simple model system. *J. Chem. Phys.*, 102(23):9285–9295, 06 1995. ISSN 0021-9606. doi:10.1063/1.468795.

[35] F. G. Eich and F. Agostini. The adiabatic limit of the exact factorization of the electron-nuclear wave function. *J. Chem. Phys.*, 145(5), August 2016. ISSN 1089-7690. doi:10.1063/1.4959962.

[36] F. Agostini and E. K. U. Gross. *Exact factorization of the electron–nuclear wave function: Theory and applications*, chapter 17, pages 531–562. John Wiley I& Sons, Ltd, 2020. ISBN 9781119417774. doi:<https://doi.org/10.1002/9781119417774.ch17>.

[37] F. Agostini and B. F. E. Curchod. When the exact factorization meets conical intersections. . . . *Eur. Phys. J. B*, 91(141):11, jul 2018. doi:10.1140/epjb/e2018-90117-6.

[38] A. Abedi, F. Agostini, Y. Suzuki, and E. K. U. Gross. Dynamical steps that bridge piecewise adiabatic shapes in the exact time-dependent potential energy surface. *Phys. Rev. Lett.*, 110: 263001, Jun 2013. doi:10.1103/PhysRevLett.110.263001.

[39] G. H. Gossel, L. Lacombe, and N. T. Maitra. On the numerical solution of the exact factorization equations. *J. Chem. Phys.*, 150(15):154112, 04 2019. ISSN 0021-9606. doi:10.1063/1.5090802.

[40] E. Lorin. Numerical analysis of the exact factorization of molecular time-dependent Schrödinger wavefunctions. *Commun. Nonlinear Sci. Numer. Simul.*, 95:105627, 2021. ISSN 1007-5704. doi:<https://doi.org/10.1016/j.cnsns.2020.105627>.

[41] J. Stetzler, S. Garashchuk, and V. Rassolov. Analysis of divergent dynamics of exactly factorized electron-nuclear wavefunctions. submitted to Philosophical Magazine in Sept 2025.

[42] Gordon H. Dunn. Photodissociation of H_2^+ and D_2^+ : Theory. *Phys. Rev.*, 172:1–7, Aug 1968. doi:10.1103/PhysRev.172.1.

[43] J D Argyros. Photodissociation of H_2^+ : Variation with temperature. *J. Phys. B*, 7(15):2025, oct 1974. doi:10.1088/0022-3700/7/15/011.

[44] J.G. Maas, N.P.F.B. van Asselt, and J. Los. Unimolecular dissociation of H_2^+ and D_2^+ . *Chem.*

Phys., 8(1):37–45, 1975. ISSN 0301-0104. doi:[https://doi.org/10.1016/0301-0104\(75\)80092-9](https://doi.org/10.1016/0301-0104(75)80092-9).

[45] J.-B. Ozenne, J. Durup, R.W. Odom, C. Pernot, A. Tabché-Fouhaillé, and M. Tadjeddine. Laser photodissociation of the isotopic hydrogen molecular ions. Comparison between experimental and ab initio computed fragment kinetic energy spectra. *Chem. Phys.*, 16(1):75–80, 1976. ISSN 0301-0104. doi:[https://doi.org/10.1016/0301-0104\(76\)89024-6](https://doi.org/10.1016/0301-0104(76)89024-6).

[46] S Saha, K K Datta, D Basu, and A K Barua. Photodissociation of H_2^+ by the $1s\sigma g \rightarrow 2p\pi u$ transition. *J. Phys. B*, 13(19):3755, oct 1980. doi:10.1088/0022-3700/13/19/013.

[47] Szczepan Chelkowski, Tao Zuo, Osman Atabek, and André D. Bandrauk. Dissociation, ionization, and coulomb explosion of H_2^+ in an intense laser field by numerical integration of the time-dependent schrödinger equation. *Phys. Rev. A*, 52:2977–2983, Oct 1995. doi: 10.1103/PhysRevA.52.2977.

[48] A Giusti-Suzor, F H Mies, L F DiMauro, E Charron, and B Yang. Dynamics of H_2^+ in intense laser fields. *J. Phys. B*, 28(3):309, feb 1995. doi:10.1088/0953-4075/28/3/006.

[49] Isao Kawata and Hirohiko Kono. Dual transformation for wave packet dynamics: Application to Coulomb systems. *J. Chem. Phys.*, 111(21):9498–9508, 12 1999. ISSN 0021-9606. doi: 10.1063/1.480281.

[50] Isao Kawata, Hirohiko Kono, and Yuichi Fujimura. Adiabatic and diabatic responses of H_2^+ to an intense femtosecond laser pulse: Dynamics of the electronic and nuclear wave packet. *J. Chem. Phys.*, 110(23):11152–11165, 06 1999. ISSN 0021-9606. doi:10.1063/1.478002.

[51] Vladimir S Lebedev, Leonid P Presnyakov, and Igor I Sobel'man. Radiative transitions in the molecular H_2^+ ion. *Phys.-Uspekhi*, 46(5):473, may 2003. doi: 10.1070/PU2003v046n05ABEH001334.

[52] Thomas Kreibich, Robert van Leeuwen, and E.K.U. Gross. Time-dependent variational approach to molecules in strong laser fields. *Chem. Phys.*, 304(1):183–202, 2004. ISSN 0301-0104. doi:<https://doi.org/10.1016/j.chemphys.2004.04.016>. Towards Multidimensional Quantum Reaction Dynamics.

[53] Hirohiko Kono, Yukio Sato, Nobuyuki Tanaka, Tsuyoshi Kato, Katsunori Nakai, Shiro Koseki, and Yuichi Fujimura. Quantum mechanical study of electronic and nuclear dynamics of molecules in intense laser fields. *Chem. Phys.*, 304(1):203–226, 2004. ISSN 0301-0104. doi: <https://doi.org/10.1016/j.chemphys.2004.04.017>.

[54] R. E. Wyatt. *Quantum dynamics with trajectories: Introduction to quantum hydrodynamics*. Springer-Verlag, 2005.

[55] D. Bohm. A suggested interpretation of the quantum theory in terms of "hidden" variables, I and II. *Phys. Rev.*, 85:166–193, 1952.

[56] S. Garashchuk, V. Rassolov, and O. Prezhdo. *Semiclassical Bohmian dynamics*, chapter 6, pages 287–368. John Wiley & Sons, Ltd, 2010. ISBN 9780470890905. doi: <https://doi.org/10.1002/9780470890905.ch6>.

[57] L Cruz-Rodríguez, Llinersy Uranga-Piña, Aliezer Martínez-Mesa, and C Meier. Interacting trajectory representation of quantum dynamics: Influence of boundary conditions on the tunneling decay of resonant states. *J. Phys. B*, 56, 01 2023. doi:10.1088/1361-6455/acb0b0.

[58] L. Dupuy, G. Parlant, B. Poirier, and Y. Scribano. Direct and accurate calculation of dwell times and time delays using quantum trajectories. *Phys. Lett. A*, 456:128548, 2022. ISSN 0375-9601. doi:<https://doi.org/10.1016/j.physleta.2022.128548>.

[59] R. Lombardini and B. Poirier. Interacting quantum trajectories for particles with spin 1/2. *Mol. Phys.*, 122(15-16):e2334805, 2024. doi:10.1080/00268976.2024.2334805.

[60] R. E. Wyatt, C. L. Lopreore, and G. Parlant. Electronic transitions with quantum trajectories.

J. Chem. Phys., 114:5113–5116, 2001.

- [61] L. Dupuy, F. Talotta, F. Agostini, D. Lauvergnat, B. Poirier, and Y. Scribano. Adiabatic and nonadiabatic dynamics with interacting quantum trajectories. *J. Chem. Theory Comput.*, 18(11):6447–6462, 2022. doi:10.1021/acs.jctc.2c00744.
- [62] S. Garashchuk, V. A. Rassolov, and G. C. Schatz. Semiclassical nonadiabatic dynamics based on quantum trajectories for the O(^3P , ^1D)+H₂ system. *J. Chem. Phys.*, 124:244307, 2006.
- [63] A. S. Sanz and S. Miret-Artés. A causal look into the quantum Talbot effect. *J. Chem. Phys.*, 126(23):234106, 2007.
- [64] Angel S. Sanz. Symmetries and singular behaviors with Bohmian trajectories. *J. Phys. Conf. Ser.*, 2883(1):012011, nov 2024. doi:10.1088/1742-6596/2883/1/012011. URL <https://dx.doi.org/10.1088/1742-6596/2883/1/012011>.
- [65] S. Garashchuk and V. A. Rassolov. Energy conserving approximations to the quantum potential: Dynamics with linearized quantum force. *J. Chem. Phys.*, 120:1181–1190, 2004.
- [66] O. V. Prezhdo. Quantized Hamilton dynamics. *Theor. Chem. Acta*, 116:206–218, 2006.
- [67] Brendan Smith and Alexey V. Akimov. Entangled trajectories Hamiltonian dynamics for treating quantum nuclear effects. *J. Chem. Phys.*, 148(14):144106, 04 2018. ISSN 0021-9606. doi:10.1063/1.5022573.
- [68] M. Dutra, S. Wickramasinghe, and S. Garashchuk. Quantum dynamics with the quantum trajectory-guided adaptable gaussian bases. *J. Chem. Theory Comput.*, 16(1):18–34, 2020. doi:10.1021/acs.jctc.9b00844.
- [69] C. C. Martens. Surface hopping without momentum jumps: A quantum-trajectory-based approach to nonadiabatic dynamics. *J. Phys. Chem. A.*, 123(5):1110–1128, 2019. doi:10.1021/acs.jpca.8b10487.
- [70] D. Han, C. C. Martens, and A. V. Akimov. Generalization of quantum-trajectory surface hopping to multiple quantum states. *J. Chem. Theory Comput.*, 21(6):2839–2853, 2025. doi:10.1021/acs.jctc.4c01751.
- [71] V. A. Rassolov and S. Garashchuk. Semiclassical nonadiabatic dynamics with quantum trajectories. *Phys. Rev. A*, 71:032511, 2005.
- [72] Sophya Garashchuk and Vitaly A. Rassolov. Chapter three - molecular dynamics with nuclear quantum effects: Approximations to the quantum force. In David A. Dixon, editor, *Annual Reports in Computational Chemistry*, volume 16, pages 41–90. Elsevier, 2020. doi: <https://doi.org/10.1016/bs.arcc.2020.07.004>.
- [73] Maple 14 and 16. Maplesoft, a division of Waterloo Maple Inc., Waterloo, Ontario.
- [74] V. A. Rassolov, S. Garashchuk, and G. C. Schatz. Quantum trajectory dynamics in arbitrary coordinates. *J. Phys. Chem. A*, 110:5530–5536, 2006.
- [75] S. Garashchuk and V. A. Rassolov. Quantum dynamics with Bohmian trajectories: Energy conserving approximation to the quantum potential. *Chem. Phys. Lett.*, 376:358–363, 2003.
- [76] M. D. Feit, J. A. Fleck, and A. Steiger. Solution of the Schrödinger equation by a spectral method. *J. Comp. Phys.*, 47(3):412–433, 1982.
- [77] R. Kosloff. Time-dependent quantum-mechanical methods for molecular dynamics. *J. Phys. Chem.*, 92:2087–2100, 1988.
- [78] V. A. Rassolov and S. Garashchuk. Bohmian dynamics on subspaces using linearized quantum force. *J. Chem. Phys.*, 120(15):6815–6825, 04 2004. ISSN 0021-9606. doi:10.1063/1.1669385.
- [79] Milton Abramowitz and Irene A. Stegun. *Handbook of mathematical functions with formulas, graphs, and mathematical tables*, volume No. 55 of *National Bureau of Standards Applied Mathematics Series*. U. S. Government Printing Office, Washington, DC, 1964.